

## RESEARCH ARTICLE

10.1002/2014JB011594

## Key Points:

- A frequency-independent 3-D  $Q_p$  model for Kilauea
- Low- $Q_p$  values at shallow depths in the summit caldera and its rift zones
- Very high  $Q_p$  values (up to 1000) at 9 km depth beneath the rift zones

## Supporting Information:

- Text S1
- Figure S1
- Figure S2

## Correspondence to:

G. Lin,  
glin@rsmas.miami.edu

## Citation:

Lin, G., P. M. Shearer, F. Amelung, and P. G. Okubo (2015), Seismic tomography of compressional wave attenuation structure for Kilauea Volcano, Hawai'i, *J. Geophys. Res. Solid Earth*, 120, 2510–2524, doi:10.1002/2014JB011594.

Received 6 SEP 2014

Accepted 6 MAR 2015

Accepted article online 12 MAR 2015

Published online 13 APR 2015

## Seismic tomography of compressional wave attenuation structure for Kilauea Volcano, Hawai'i

Guoqing Lin<sup>1</sup>, Peter M. Shearer<sup>2</sup>, Falk Amelung<sup>1</sup>, and Paul G. Okubo<sup>3</sup>

<sup>1</sup>Department of Marine Geosciences, Rosenstiel School of Marine and Atmospheric Science, University of Miami, Miami, Florida, USA, <sup>2</sup>Institute of Geophysics and Planetary Physics, Scripps Institution of Oceanography, University of California, San Diego, La Jolla, California, USA, <sup>3</sup>Hawaiian Volcano Observatory, U.S. Geological Survey, Hawaii Volcanoes National Park, Hawaii, USA

**Abstract** We present a frequency-independent three-dimensional (3-D) compressional wave attenuation model (indicated by the reciprocal of quality factor  $Q_p$ ) for Kilauea Volcano in Hawai'i. We apply the simul2000 tomographic algorithm to the attenuation operator  $t^*$  values for the inversion of  $Q_p$  perturbations through a recent 3-D seismic velocity model and earthquake location catalog. The  $t^*$  values are measured from amplitude spectra of 26708  $P$  wave arrivals of 1036 events recorded by 61 seismic stations at the Hawaiian Volcanology Observatory. The 3-D  $Q_p$  model has a uniform horizontal grid spacing of 3 km, and the vertical node intervals range between 2 and 10 km down to 35 km depth. In general, the resolved  $Q_p$  values increase with depth, and there is a correlation between seismic activity and low- $Q_p$  values. **The area beneath the summit caldera is dominated by low- $Q_p$  anomalies throughout the entire resolved depth range.** The Southwest Rift Zone and the East Rift Zone exhibit very high  $Q_p$  values at about 9 km depth, whereas the shallow depths are characterized with low- $Q_p$  anomalies comparable with those in the summit area. The seismic zones and fault systems generally display relatively high  $Q_p$  values relative to the summit. The newly developed  $Q_p$  model provides an important complement to the existing velocity models for exploring the magmatic system and evaluating and interpreting intrinsic physical properties of the rocks in the study area.

## 1. Introduction

Seismic velocities and  $V_p/V_s$  ratios vary with many factors, such as composition, saturation, temperature, pressure, mineralogy, and petrology [e.g., Alexandrov and Ryzhova, 1961; Kern, 1982; Christensen and Mooney, 1995; Christensen, 1996; Trampert et al., 2001; Lee, 2003]. In the crust, composition may be the most fundamental factor. Attenuation of seismic waves supplies additional constraints on Earth's anelastic properties, which are affected by temperature and fluid content [Jackson and Anderson, 1970], properties that are especially important for the exploration and evaluation of volcanic systems. However, attenuation inversions are less common than velocity studies mainly because of data scatter, inversion complexity, and interpretation difficulty. Previous seismic attenuation tomographic inversions have been performed for the Medicine Lake Volcano of Northern California Cascade Range [Evans and Zucca, 1988], Yellowstone Caldera [Clawson et al., 1989], Newberry Volcano of Central Cascade Range [Zucca and Evans, 1992], Long Valley Caldera of California [Sanders, 1993; Ponko and Sanders, 1994; Sanders et al., 1994, 1995; Sanders and Nixon, 1995], Mount Etna and Mount Vesuvius in Italy [Martinez-Arevalo et al., 2005; De Gori et al., 2005; Del Pezzo et al., 2006; De Siena et al., 2009], and Okmok Volcano, Alaska [Ohlendorf et al., 2014]. These attenuation results are usually interpreted together with the velocity structure. Lees [2007] presented a thorough review of seismic tomography in volcanic regions and summarized that low velocity and high attenuation are commonly attributed to magma accumulation and high velocity and low attenuation to cooled magma dikes or extinct chambers.

Kilauea Volcano in Hawai'i (Figure 1) has served as a natural laboratory for studying seismic and volcanic activity for the past few decades [e.g., Swanson et al., 1976a; Lipman et al., 1985; Hill and Zucca, 1987; Rubin et al., 1998; Cayol et al., 2000; Hill et al., 2002; Amelung et al., 2007; Brooks et al., 2008; Poland et al., 2014]. Numerous studies have been carried out to investigate the crust and upper mantle velocity structure under Kilauea [e.g., Ryall and Bennett, 1968; Hill, 1969; Ellsworth and Koyanagi, 1977; Thurber, 1984; Rowan and Clayton, 1993; Okubo et al., 1997; Dawson et al., 1999; Haslinger et al., 2001; Hansen et al., 2004;

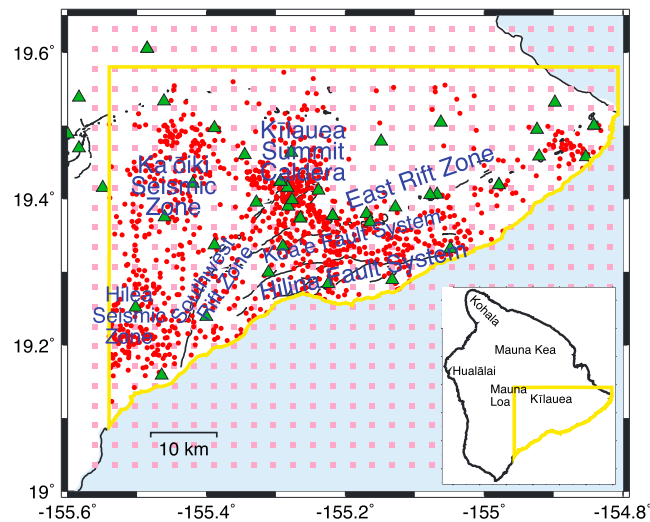


**Figure 1.** Seismic events (dots), stations (triangles), and model grid (pink squares) used in the  $Q_p$  tomographic inversion for the study area enclosed by the yellow polygon. Major geological structures include Kilauea Summit Caldera, the Southwest and East Rift Zones, the Koa'e and Hilinea Fault Systems, and the Ka'ōiki and Hilea Seismic Zones. Inset map shows the location of our study area on the Hawai'ian Islands.

Monteiller et al., 2005; Park et al., 2007; Got et al., 2008; Park et al., 2009; Syracuse et al., 2010; Lin et al., 2014a). A common feature of these models is the high compressional ( $P$ ) velocity anomalies at intermediate depths (5–10 km) below the summit caldera and its rift zones.

Compared to the extensive velocity studies, much less attention has been paid to the attenuation structure in Kilauea. Ho-Liu [1988] used shear to compressional wave amplitude ratios to invert for seismic attenuation variations in Kilauea and its East Rift Zone (ERZ) and found attenuating anomalies associated with the shallow magma chamber and the ERZ. Hansen et al. [2004] conducted three-dimensional (3-D) velocity and attenuation model inversions for the East Rift Zone and south flank of Kilauea.

The main result of their study was

identification of an anomalous body with low- $P$  velocity ( $V_p$ ), low compressional to shear wave velocity ratio ( $V_p/V_s$ ), high- $P$  quality factor ( $Q_p$ ), and low- $S$  quality factor ( $Q_s$ ) at ~7 km depth beneath the ERZ, which was interpreted as a trapped  $CO_2$  reservoir.

In this paper, we present a frequency-independent 3-D  $P$  wave attenuation model (indicated by the inverse of quality factor  $Q_p$ ) for Kilauea Volcano. The newly developed  $Q_p$  model provides a useful complement to the existing velocity models for understanding the structural heterogeneity, thermal conditions, and fluid saturation of rocks in the study area.

## 2. Tomographic Inversion Method

We apply the simul2000 inversion method and algorithm [Thurber, 1993; Eberhart-Phillips and Michael, 1993; Thurber and Eberhart-Phillips, 1999] to solve for  $Q_p$  variations at 3-D grid nodes. During the attenuation inversion, the frequency-independent attenuation operator  $t^*$  values, usually determined from the high-frequency decay rate of direct-wave amplitude spectra, are inverted for 3-D  $Q_p$  structure by tracing the raypaths through a given velocity model. The relationship between  $t^*$  and  $Q_p$  for the raypath between event  $i$  and station  $j$  can be expressed as

$$t_{ij}^* = \int_{ij} \frac{1}{Q_p(x, y, z) \times V_p(x, y, z)} ds + t_{station}^* \quad (1)$$

where  $V_p$  is the  $P$  wave velocity model and  $ds$  is an element of path length. The local site effect can be described by a station constant  $t_{station}^*$  operator that can be included in the inversion [Anderson and Hough, 1984]. However, we did not invert for station terms in this study to avoid trade-offs with other model parameters and to avoid projecting resolvable shallow attenuation structure into the station corrections. This is also consistent with the inversion process for the velocity model used in this study [Lin et al., 2014a], in which station corrections were also not calculated. The simul2000 algorithm solves equation (1) for  $Q_p$  iteratively since the inversion is nonlinear. It uses a combination of parameter separation [Pavlis and Booker, 1980; Spencer and Gubbins, 1980] and damped least squares inversion to solve for model perturbations. The optimal damping parameter is selected empirically using a data misfit versus model variance trade-off analysis. A full resolution matrix for the solution can also be calculated to evaluate the quality of the model.

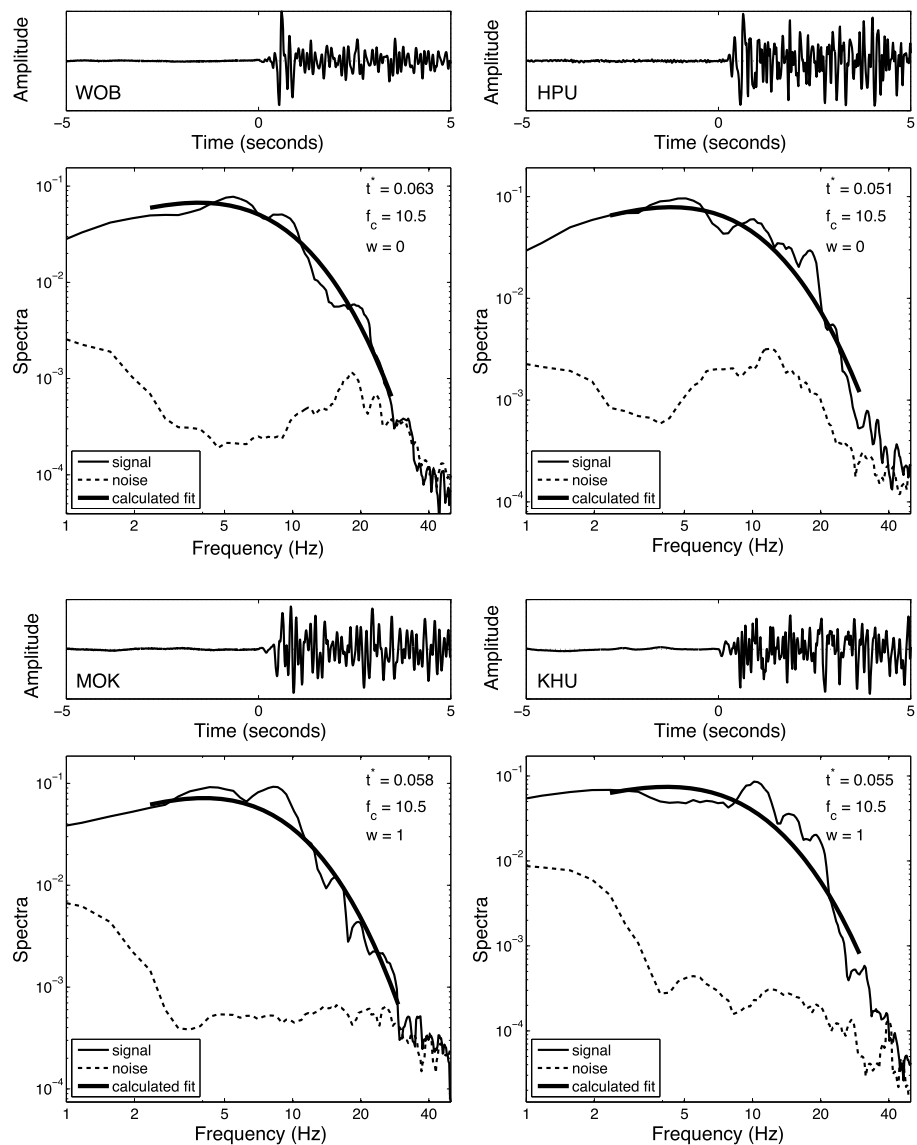


**Figure 2.** Examples of time series and amplitude spectra, along with the computed  $t^*$  values, corner frequencies, and assigned weights.

### 3. Data and Processing

The original seismic data used in this study, including the earthquake catalog, phase arrival times, and waveform data from 61 seismic stations, were obtained from the Hawaiian Volcanology Observatory (HVO). We select events from the subset of earthquakes with magnitudes between 2 and 5 for the tomographic inversion in order to exclude smaller events that may have low signal levels and larger events that are usually characterized with complex source time functions.

During the attenuation inversion as shown by equation (1), earthquakes are fixed at the input locations and  $t^*$  values are inverted for  $Q_p$  variations through 3-D ray tracing of a given velocity model, preferably a 3-D model. In this work, we use the most recent 3-D velocity model by Lin *et al.* [2014a] for the 3-D ray tracing, which covers the entire island of Hawai'i with 3 km horizontal node spacing and 2 to 10 km node spacing in depth. The event locations are from the earthquake catalog relocated by using the 3-D ray tracing, similar event cluster analysis, and waveform cross-correlation methods in the same study.

We determine  $t^*$  values from  $P$  wave spectra recorded by the vertical component of the HVO seismic stations. The amplitude spectrum is calculated for a 2.56 s time window around each  $P$  arrival time by using

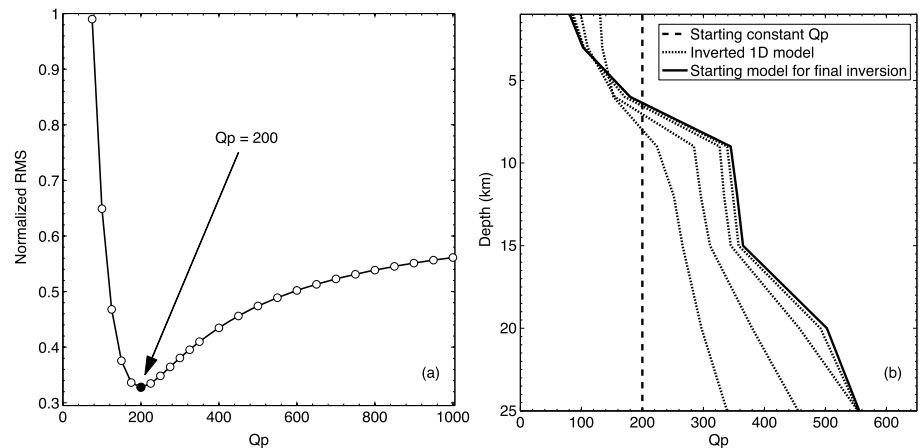


**Figure 3.** (a) Initial constant  $Q_p$  determined by the root-mean-square (RMS) of the attenuation operator  $t^*$  residuals. The RMS ranges from 0.060 to 0.020 and reaches the minimum value at  $Q_p = 200$ . (b) Examples of the 1-D  $Q_p$  models. Dashed line shows the constant  $Q_p$  value of 200. Dotted lines are examples of the 1-D models during the model selection. The RMS drops from 0.020 to 0.015. Solid line is the starting 1-D model for the inversion of the final 3-D tomography model.

the multitaper approach of *Prieto et al.* [2009]. A corresponding noise spectrum is also computed for a 2.56 s window immediately before the signal segment. Here we follow the techniques and notation in *Rietbrock* [2001] and *Eberhart-Phillips and Chadwick* [2002] for the determination of  $t^*$  values. If we assume an  $f^{-2}$  source model [*Brune, 1970*], the velocity amplitude spectrum  $A_{ij}(f)$  of event  $i$  at station  $j$  can be expressed as

$$A_{ij}(f) = 2\pi f \Omega_{0ij} \frac{f_{ci}^2}{f_{ci}^2 + f^2} \exp[-\pi f t_{ij}^*] \quad (2)$$

where  $\Omega_{0ij}$  is the long-period amplitude,  $f_{ci}$  is the source corner frequency of event  $i$ , and  $t_{ij}^*$  is the frequency-independent attenuation operator. The  $\Omega_{0ij}$  term includes a geometrical spreading factor. However, amplitude also depends on the focusing/defocusing of rays by the heterogeneous velocity structure, which can be described by the second derivative of the traveltime curve and is complicated to quantify. We determine these unknown parameters using an iterative spectral-fitting method. The best fitting corner frequency is defined as the frequency that minimizes the difference between the observed and calculated velocity spectra, which is used to calculate the final  $t_{ij}^*$  and  $\Omega_{0ij}$  values. During the fitting, we also assign weights of 0 (best fitting), 1, 2, 3, and 4 (worst fitting) to each observation according to the individual fitting error compared with the overall misfit, which are used for the tomographic inversion.

In this study, we only use measurements with a signal-to-noise ratio above 2 in a continuous 10 Hz wide frequency band between 2 and 30 Hz. Source corner frequency is grid searched between 2 and 20 Hz. Figure 2 shows examples of velocity amplitude spectra and  $t^*$  for an event. After the determination of  $t^*$  values, we select events with at least 10  $t^*$  values with weights smaller than 3 and separated by 1 km as the input for the tomography inversion. This results in 1036 events and 26,708  $t^*$  values. These seismic events are shown by the red dots in Figure 1.

For the final  $Q_p$  model in this study, we use the same grid node as that for the 3-D velocity model by *Lin et al.* [2014a] with a horizontal grid spacing of 3 km (squares in Figure 1) and vertical intervals ranging between 2 and 10 km from  $-1$  to 35 km depth. Note that in this study all depths are relative to mean sea level. In seismic velocity and attenuation tomography, 3-D model inversions are usually found strongly dependent on the initial models, especially when one-dimensional (1-D) models are used as starting models. Therefore, we started by searching for an optimal 1-D model in order to obtain a robust final model. We first ran a series of single-iteration inversions through uniform half-space models with varying  $Q_p$  values and chose the one that gives the minimum data misfit as the best constant  $Q_p$  value. Figure 3a shows that 200 gives the minimum root-mean-square (RMS) of data misfit with the RMS varying from 0.060 to 0.020 s for the range of  $Q_p$  between 75 and 1000. Values beyond this range significantly increase the data misfit and destabilize the inversion process. Next we used 200 as the starting  $Q_p$  value to run another set of single-iteration

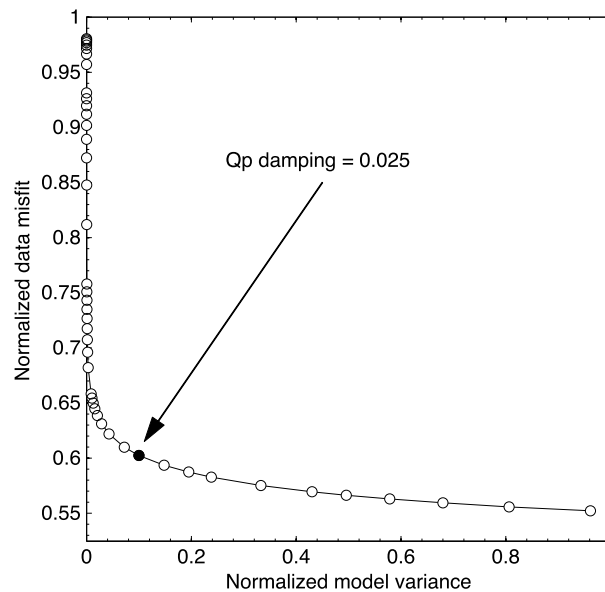


**Figure 4.** Trade-off curve between data misfit and model variance for  $Q_p$  inversion. The optimal damping parameter is selected as 0.025.

series and then the layer average values of the resulting model as the starting model for the next iteration. This process was repeated a few times until the layer average attenuation values of the inverted model were not significantly different from the input model, and they fit the data equally well. The RMS of data misfit was reduced from 0.020 to 0.015 s during this process. This final 1-D model is used as the starting model for the final attenuation inversion shown in this paper. Figure 3b shows examples of the above 1-D  $Q_p$  models.

Damping parameters are usually applied to stabilize the inversion process [e.g., Eberhart-Phillips, 1986, 1993]. The optimal damping for  $Q_p$  is selected empirically by running a series of inversions with a large range of damping values and plotting the

data misfit versus model variance trade-off curves, similar to the approach applied to the velocity model inversion [e.g., Lin et al., 2007; Lin and Thurber, 2012; Lin, 2013]. Figure 4 shows that 0.025 produced a good compromise between data misfit and model variance and was used for the final attenuation inversion.

#### 4. Synthetic Data Tests

To examine the recovering ability of our algorithms and data coverage, we performed two types of synthetic data tests in this study, a checkerboard and a restoration resolution test, similar to those for the velocity model inversions [e.g., Thurber et al., 2009; Lin et al., 2010]. In the checkerboard test, we perturbed the starting 1-D  $Q_p$  model by  $\pm 30\%$  across three grid nodes and alternating at depth. We then computed the synthetic  $t^*$  values through the perturbed model for the same distributions of event hypocenters, station locations, and  $t^*$  raypaths as the real data. Map views and cross sections of the true and inverted  $Q_p$  models are shown in Figure 5. The white contours enclose the regions where the diagonal element of the resolution matrix is greater than 0.1 (1.0 represents the best resolution and 0.0 not resolved at all). The checkerboard images in these areas are recovered and are considered to be well resolved. The model is poorly resolved at 1 km depth with the overall overestimated  $Q_p$  values therefore is not shown in the map view but is visible in the cross sections. Between 3 and 12 km depth, the model is generally well resolved, although smearing can be seen in both map views and cross sections. The highest resolution values ( $\sim 0.70$ ) appear at shallow layers (above 3 km depth), but mainly as single-node attenuation anomalies. The best recovery, in general, occurs in the 6 and 9 km depth layers ( $\sim 0.58$ ) and near the Koa'e and Hilina Fault Systems (1'-1'') owing to the great seismic activity in this depth range. The Southwest Rift Zone (A-A') and East Rift Zone (B-B') are recovered with relatively good resolution, whereas the  $Q_p$  values in the vicinity of the summit caldera seem to be overestimated relative to the true model. The Ka'oiiki Seismic Zone (1-1') is resolved with great smearing. We also calculated the correlation coefficients between the inverted model and the true model, which are 0.69, 0.70, 0.88, and 0.93 for the well-resolved areas of the four layers at 3, 6, 9, and 12 km depth shown in the map views. Although the correlation at 12 km depth is the highest, the resolved area is limited to the summit caldera area.

In the restoration test, event hypocenters, station locations and ray geometries also have the same distributions as the real data. Synthetic  $t^*$  values are calculated from the final inverted 3-D model resulting from the real data. We add Gaussian distributed noise with zero mean and 0.01 s standard deviation to simulate random errors in  $t^*$  measurements. We followed the same inversion strategies and applied the same inversion parameters, such as the damping parameter, as those for the real data. The inverted model

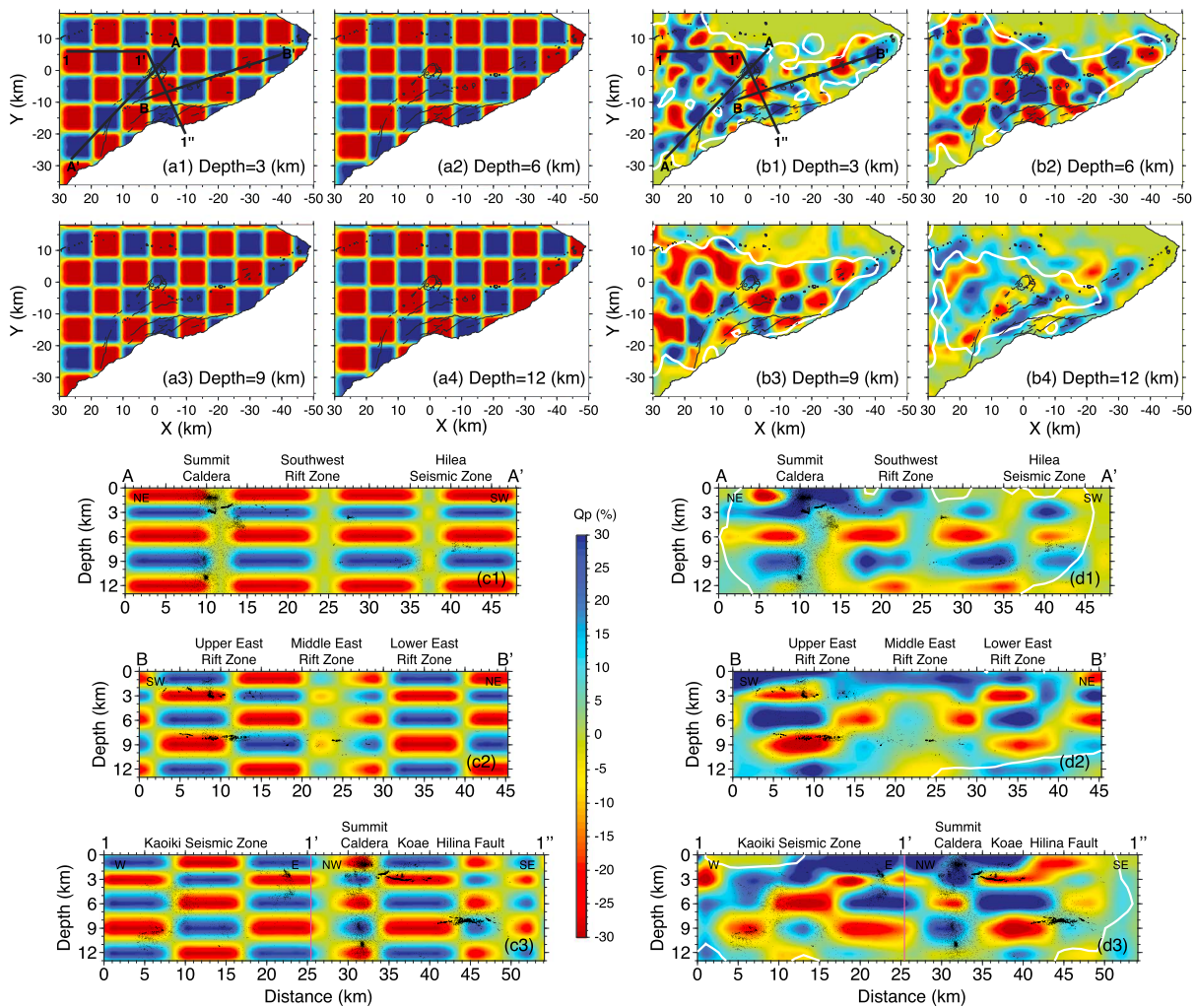


**Figure 5.** Checkerboard resolution test for the  $Q_p$  model. (a1–a4) Map views of the true model. Black straight lines show profile locations for the cross sectional views in Figures 5c1–5c3 and 5d1–5d3. Note that these profiles are not parallel or perpendicular to the grid coordinates; therefore, the  $Q_p$  perturbations are not exactly alternating across the inversion grids. (b1–b4) Map views of the inverted model. (c1–c3) Cross sections of the true model along profiles A–A', B–B', and 1–1', respectively. (d1–d3) Cross sections of the inverted model along the same profiles. The black dots represent the waveform cross-correlation relocated earthquakes from Lin *et al.* [2014a] within  $\pm 5$  km of the profile. The white contours in the inverted model enclose the areas where the diagonal element of the resolution matrix is greater than 0.1. Black lines in map views denote the coast line and surface traces of mapped faults.

is similar to the true model in the well-resolved areas (Figure 6) and the RMS reduction of the  $t^*$  residuals matches that seen in the real data. The correlation coefficients for the well-resolved areas between the inverted model and the true model are 0.85, 0.86, 0.89 and 0.96 at 3, 6, 9, and 12 km depth. Both the checkerboard and restoration tests show that the model recovery is generally good in our study area, with the best resolution in the regions with abundant seismicity, such as the Koa'e and Hilina Fault Systems.

## 5. Results

The final tomographic inversion converges after five iterations. The RMS of the  $t^*$  residuals drops from 0.015 to 0.010 s after the inversion (Figure 7). This amount of reduction is comparable with other local-/regional-scale attenuation studies [e.g., Eberhart-Phillips and Chadwick, 2002; Hauksson and Shearer, 2006; Bennington *et al.*, 2008; Nakajima *et al.*, 2013; Lin, 2014a, 2014b].

In Figure 8, we show the map view slices of the  $Q_p$  model at four different layer depths from 3 to 12 km below sea level. At 3 km depth,  $Q_p$  values range from 25 to 310 with the lowest value (i.e., highest attenuation) in the summit caldera and the highest value (i.e., lowest attenuation) in the Hilea Seismic Zone.

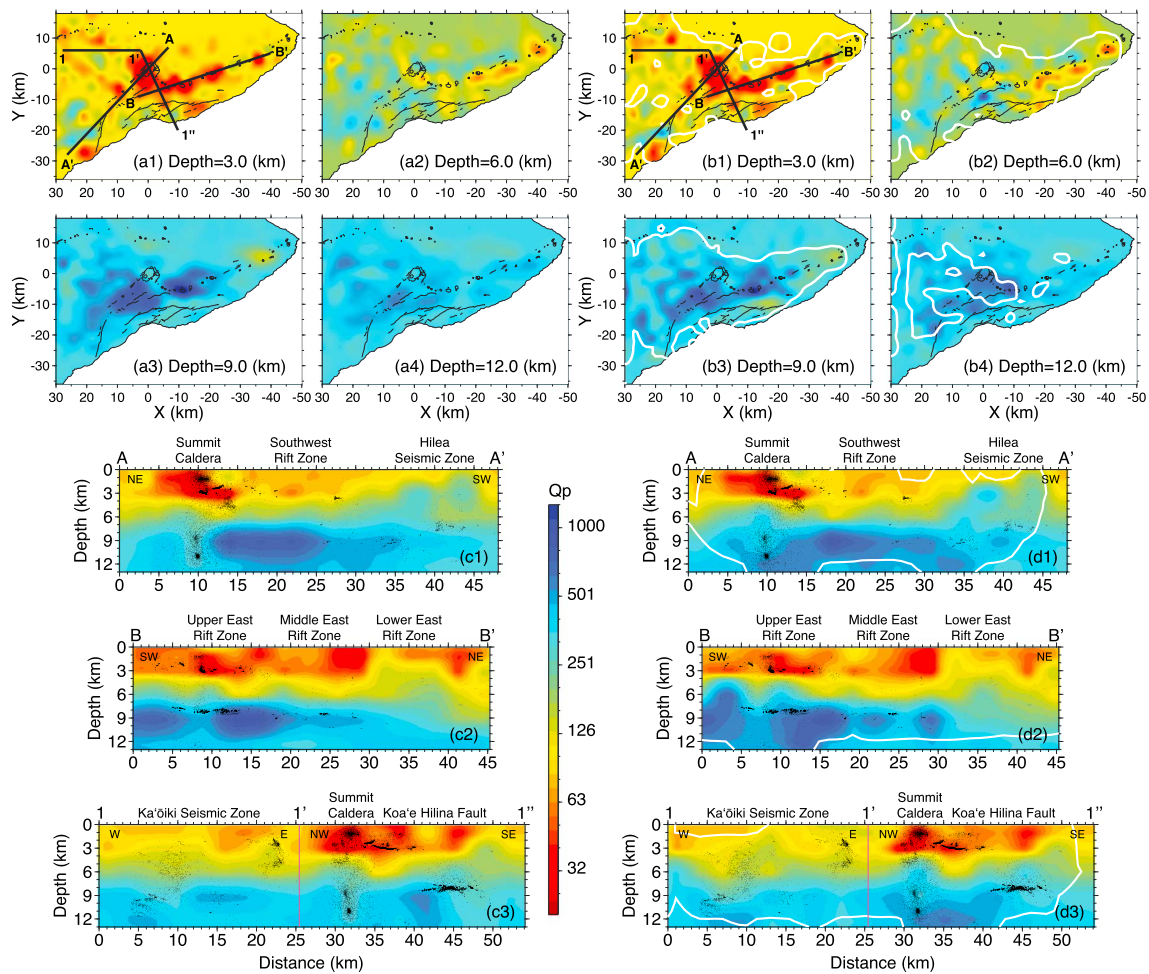


**Figure 6.** Restoration resolution test with Gaussian distributed random noise for the  $Q_p$  model. (a1–a4) Map views of the true model. Black straight lines show profile locations for the cross sectional views in Figures 6c1–6c3 and 6d1–6d3. (b1–b4) Map views of the inverted model. (c1–c3) Cross sections of the true model along profiles A-A', B-B', and 1-1', respectively. (d1–d3) Cross sections of the inverted model along the same profiles. The black dots represent the waveform cross-correlation relocated earthquakes from *Lin et al.* [2014a] within  $\pm 5$  km of the profile. The white contours in the inverted model enclose the areas where the diagonal element of the resolution matrix is greater than 0.1. Black lines in map views denote the coast line and surface traces of mapped faults.

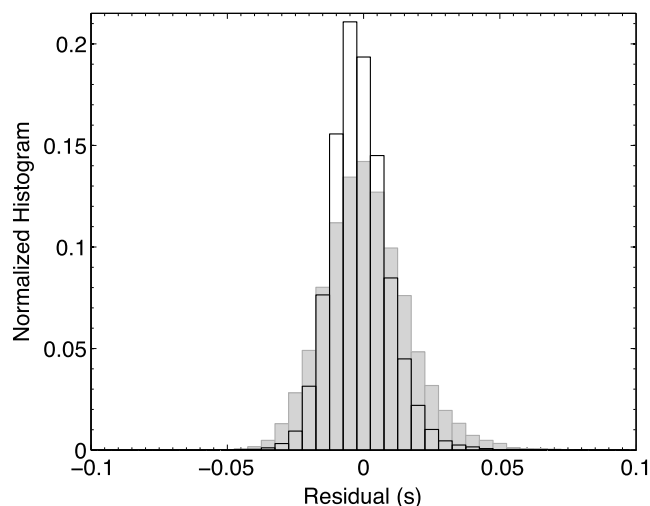


**Figure 7.** The  $t^*$  residual distribution for the starting (gray) and final (black-white)  $Q_p$  models. The root-mean-square of the  $t^*$  residuals drops from 0.015 s to 0.010 s for the events used in the inversion.

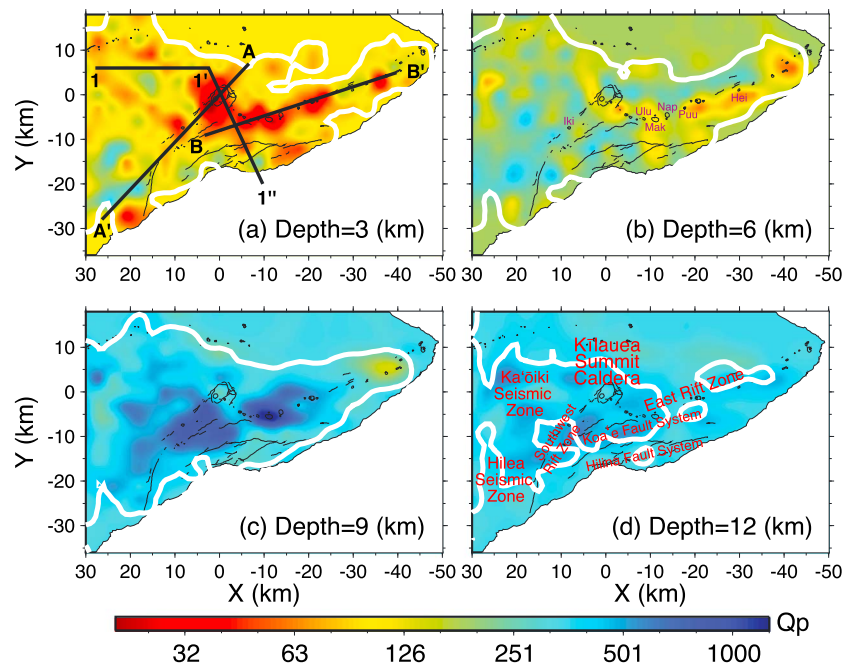


**Figure 8.** (a–d) Map views of the  $Q_p$  model at different depth slices. The white contours enclose the areas where the diagonal element of the resolution matrix is greater than 0.1. Black straight lines in Figure 8a show profile locations for the cross sections in Figure 9, same as those in Figures 5 and 6. Major craters in Figure 8b are Iki: Mauna Iki; ULU: Mauna Ulu; Mak: Makaopuhi; Nap: Nāpau; Puu: Pu'u'Ō'ō; and Hei: Heiheiahulu. Main geological structures are marked in Figure 8d. Black lines denote the coast line and surface traces of mapped faults.

The rift zones are generally dominated by low- $Q_p$  values ( $\sim 40$ – $50$ ), and the Hilina Fault Zone is seen with relatively high values ( $\sim 160$ ). At 6 km depth, the  $Q_p$  values are relatively uniform on the west side of the study area ( $x = 30$ – $0$  km) with an average value of 204. The highest- $Q_p$  values of up to 450 are again observed in the Ka'ōiki and Hilea Seismic Zones. The East Rift Zones are dominated by low values with the lowest of  $\sim 90$  in the Lower ERZ. The highest- $Q_p$  values (i.e., lowest attenuation) of  $\sim 1200$  in the entire study area are seen at 9 km depth in the Southwest Rift Zone and Upper and Middle East Rift Zones. Small low- $Q_p$  values are observed in the Lower East Rift Zone and the Hilina Fault Zone. Starting from 12 km depth, the model resolution is limited with only the vicinity of the summit caldera well resolved, where the low- $Q_p$  values of  $\sim 355$  near the caldera are surrounded by high- $Q_p$  bodies of  $\sim 562$ .

We also plot the  $Q_p$  variations in three cross sections through the new model (Figure 9). Profile A-A' cuts through Kīlauea's summit caldera and its Southwest Rift Zone (SWRZ). The caldera area is dominated by relatively low  $Q_p$  values throughout the entire depth range compared with other regions in this cross section. The seismicity is well correlated with the low  $Q_p$  values, defining the path of the magma ascent. The Southwest Rift Zone is seen with relatively high  $Q_p$  values. The highest values of up to 1000 are observed between 8 and 12 km depth, coincident with an aseismic zone. As seen in the map views, relatively high  $Q_p$  values at shallow depths (above 6 km depth) are seen in the Hilea Seismic Zone. Along profile B-B' through Kīlauea's East Rift Zone, the  $Q_p$  values are generally lower than those in the Southwest Rift Zone above 4 km depth, consistent with the continuous magmatic activity here. The Lower ERZ with sparse seismicity displays slightly higher  $Q_p$  values above 6 km depth than the Upper and Middle Rift Zones. Similar to the Southwest Rift Zone, high  $Q_p$  values are resolved between 8 and 12 km depth beneath the south flank and Upper East Rift Zone. The seismicity is relocated as subhorizontal linear features right above these high- $Q_p$  bodies. The next cross section 1-1'-1'' goes through the Ka'ōiki Seismic Zone, summit caldera, and the Koa'e and Hilina Fault Systems. The Ka'ōiki Seismic Zone (1-1') shows relatively uniform  $Q_p$  variations compared to the summit caldera and fault systems. As seen in A-A', seismicity beneath the summit caldera coincides with relatively low  $Q_p$  values throughout the entire depth range. Seismicity associated with a subhorizontal décollement is relocated at 8 km depth above a high- $Q_p$  body.

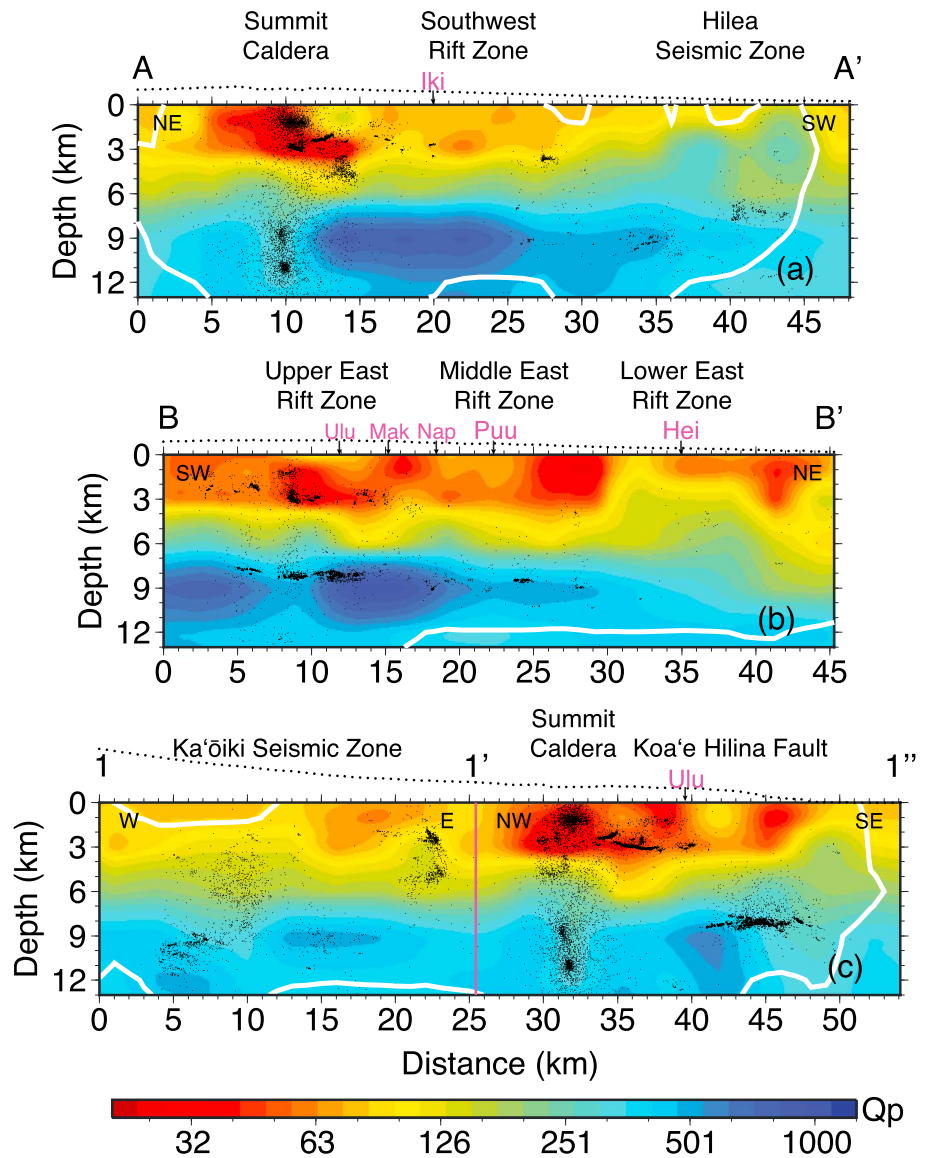


**Figure 9.** (a–c) Cross sections of the  $Q_p$  model along the three profiles shown in Figure 8. The black dots represent the waveform cross-correlation relocated earthquakes from Lin *et al.* [2014a] within  $\pm 5$  km of the profiles. The white contours enclose the area where the diagonal element of the resolution matrix is greater than 0.1. Dotted curves at top illustrate the local topography. Pink texts are abbreviations for major craters in the study area, Iki: Mauna Iki; Ulu: Mauna Ulu; Mak: Makaopuhi; Nap: Nāpau; Puu: Pu'u'Ō'ō; and Hei: Heiheiahulu.

## 6. Discussion

Generally, the  $Q_p$  values in this study increase with depth (Figure 3b); i.e., attenuation decreases with depth, consistent with the increasing confining pressure. As shown in Figure 3a, the constant  $Q_p$  value that gives the minimum RMS of the  $t^*$  residuals is 200 based on an  $f^{-2}$  source model [Brune, 1970], which is significantly smaller than the values for tectonically active regions such as California. For comparison, the minimum constant  $Q_p$  value is 400 for Northern California [Lin, 2014a] and 450 for the Salton Trough in Southern California [Lin, 2014b], when an  $f^{-2}$  source model is assumed. The low-constant  $Q_p$  value in this study indicates the generally high attenuation in Kilauea, which is expected for magmatic systems [Lees, 2007]. The range of the  $Q_p$  values are similar to those in other volcanic areas with the lowest value (below 30) beneath the caldera and relatively higher values outside of the caldera [e.g., Clawson *et al.*, 1989; Ponko and Sanders, 1994; Sanders *et al.*, 1995; Martinez-Arevalo *et al.*, 2005; De Gori *et al.*, 2005].

In order to reduce ambiguities in the interpretations of the  $Q_p$  results, we discuss the main features in the  $Q_p$  model together with the  $V_p$  and  $V_p/V_s$  models from *Lin et al.* [2014a]. Cross sections of the velocity model along the three profiles in Figure 8 are available in Figure S1 in the supporting information.

### 6.1. Summit Caldera

One of the most noticeable features in the  $Q_p$  model is the overall low values (i.e., high attenuation) beneath the summit caldera compared with the surrounding areas (Figure 9a). The low- $Q_p$  values ranging from 25 to 310 are observed throughout the entire resolved depth range (from the surface to 12 km depth). Above 4 km depth, the lowest  $Q_p$  values in the study area are observed with the corresponding low- $V_p$  and low- $V_p/V_s$  ratios (Figures S1a and S1d; see Figures 12e and 12f in *Lin et al.* [2014a] for the close-up views of the shallow structure). Several previous studies have attributed the low- $V_p$  zones to magma bodies [e.g., *Thurber*, 1984, 1987; *Rowan and Clayton*, 1993; *Dawson et al.*, 1999; *Park et al.*, 2007, 2009]. Although the low- $Q_p$  values support this interpretation, the low- $V_p/V_s$  ratios are more consistent with the presence of cracks, water, and gas. **This suggests that the magma reservoir inferred from geodetic and petrologic studies [Pietruszka and Garcia, 1999; Baker and Amelung, 2012; Poland et al., 2014] is smaller than the resolvable scale of the tomographic study by Lin et al. [2014a] and surrounded by gas and/or water.** Below 4 km depth the  $Q_p$  values are still relatively low and gradually increase to about 310 at 12 km depth. The abundant seismicity coincident with the low- $Q_p$  values defines the pathways of magma ascent. This low  $Q_p$  structure has very high corresponding  $V_p$  (7–7.5 km/s) and low normal  $V_p/V_s$  values. These structural variations are consistent with the interpretation of a combination of different mafic compositions (olivine-rich gabbro and dunite) by *Lin et al.* [2014a] but may also be affected by heat, fractures, and fluid.

### 6.2. Rift Zones

Along the East Rift Zone (Figure 9b), the Upper East Rift Zone (UERZ) is the most seismically active portion. Above 4 km depth, the low- $Q_p$  values are comparable with those in the caldera area. The corresponding  $V_p$  model does not show obvious anomalies, whereas  $V_p/V_s$  ratios are very low near the surface and high between 2 and 4 km depth. The latter together with the low- $Q_p$  values are consistent with elevated temperature or even the presence of melt in this area, as are the discrete, low-resistivity bodies observed at depths of 5 km beneath the surface (i.e., 4 km below sea level) by *Kauahikaua et al.* [1986]. Localized uplift observed in the Makaopuhi crater area in the 1960–1970s is also an indication for the presence of one or more secondary magma reservoirs in the area [*Swanson et al.*, 1976b]. The low- $Q_p$  values at shallow depths together with the active seismicity are consistent with the shallow intrusions in this area. Between 4 and 8 km depth, the  $Q_p$  model does not show strong variations along the entire ERZ with values comparable to those in the summit area. Sparsely distributed seismicity is seen in the UERZ along with high  $V_p$  and low  $V_p/V_s$  at this depth range relative to the Middle and Lower East Rift Zones, which are also similar to the features beneath the caldera. Below 8 km depth, the UERZ is dominated by very high  $Q_p$ , high  $V_p$ , and high  $V_p/V_s$  ratios together with the subhorizontal seismicity, indicating cooled magma or highly competent material that may control the interaction between the summit caldera and the ERZ and the magma ascent and evolution in Kilauea. The  $Q_p$  and velocity variations are much simpler in the Middle East Rift Zone (MERZ). The  $Q_p$  values generally fall between those in the UERZ and the Lower East Rift Zone (LERZ), whereas low  $V_p$  and low  $V_p/V_s$  are seen throughout the entire depth range. The LERZ is not seismically as active as the UERZ and MERZ, and the  $V_p/V_s$  model is only well resolved at shallow depths. Above 6 km depth, the structures are complex with both high- and low- $Q_p$  and  $V_p/V_s$  ratios and slightly low  $V_p$  values. Low- $Q_p$  values are observed below 6 km depth compared to the UERZ. The  $V_p$  values are lower than the UERZ but higher than the MERZ, whereas the  $V_p/V_s$  model is not resolved at deep layers.

The  $Q_p$  values in the Southwest Rift Zone (Figure 9a) are higher than those in the summit area and the East Rift Zone throughout the entire depth range. The  $V_p$  values are generally lower than the summit values except for the depth range between 1 and 4 km where the summit magma reservoir is located. The  $V_p/V_s$  model shows normal low values (1.68–1.74) with the exception of a high  $V_p/V_s$  anomaly between 5 and 10 km depth ( $x = 15$ –22 km) that extends to the summit at shallow depths. The relatively high  $Q_p$  values in the SWRZ are consistent with the more quiescent activity here compared to the summit caldera and the ERZ. The most significant feature in this rift zone is an aseismic zone between 7 and 12 km depth ( $x = 12$ –26 km) with very high  $Q_p$ , high  $V_p$ , and high  $V_p/V_s$ , indicative of cooled magma or high-strength material in this area.

### 6.3. Crustal Magma Body

*Lin et al.* [2014b] interpreted an anomalous body with low- $V_p$ , low- $V_s$ , and high- $V_p/V_s$  values at 8–11 km depth beneath Mauna Ulu to be a crustal magma reservoir and suggested the presence of 10% melt using petrophysical models. We plot the  $Q_p$  model along the same profile as that in *Lin et al.* [2014b] in supporting information Figure S2. The  $Q_p$  values for the proposed magma reservoir are relatively high, instead of low as expected for magma accumulation. The low  $V_p$  and high  $V_p/V_s$  can be explained only by the presence of either melt or water. However, at the pressure and temperature conditions of the interested depths, it is doubtful that large amount of water would exist. *Winkler and Nur's* [1979] experiment showed that although attenuation increases (i.e.,  $Q_p$  decreases) with water saturation, fully saturated rocks show  $Q_p$  as high as dry rocks. We expect similar behavior for melt-saturated rocks where the magma reservoir is fully saturated with melt, although lab experiments are needed to confirm this.

### 6.4. Seismic Zones and Fault Systems

The seismic zones show distinctly different attenuation structures than those in Kilauea's summit caldera and its rift zones. In the Ka'ōiki Seismic Zone (Figure 9c), the  $Q_p$  values are generally higher than those in the summit area. The  $V_p$  values above 1 km are lower than those in the summit area, but higher between 1 and 4 km depth where the summit magma reservoir is located, and lower again below 4 km depth. The  $V_p/V_s$  model is dominated by low values above 6 km and shows high ratios below that. There seems to be a correlation between the  $Q_p$  and  $V_p/V_s$  models in this area, especially above 9 km depth. This is expected since both parameters are sensitive to the presence of pore fluid, which is a more dominating attenuation mechanism at shallow depths [*Winkler and Nur*, 1979]. *Scherbaum and Wyss* [1990] inverted the  $Q_p$  model in the Ka'ōiki area and observed a low ( $\sim 105$ ) volume to a depth of 5 km and increased  $Q_p$  to  $\sim 160$  between 9 and 11 km, which are slightly lower than our results.

In the Hilea Seismic Zone south of the Ka'ōiki, the  $Q_p$  values above 6 km depth are higher than those in the Ka'ōiki Seismic Zone, which is consistent with the more active seismicity in Ka'ōiki and the sparse seismicity in Hilea. Below 6 km depth, the  $Q_p$  values and seismic activity are comparable with those in the Ka'ōiki Seismic Zone.

The structures in the Hilina and Koa'e Fault Systems are much simpler, with dominantly low  $Q_p$ , low  $V_p$ , and low  $V_p/V_s$ , consistent with the inferred presence of volatiles by *Lin et al.* [2014a]. Below 4 km depth, the  $Q_p$  variations with depth are very similar to those in the Ka'ōiki Seismic Zone, consistent with the previously suggested similar origins of these two systems [*Park et al.*, 2007; *Lin et al.*, 2014a].

### 6.5. Attenuation Versus Velocity

In order to examine the relationship between the 3-D  $Q_p$  model and the velocity model by *Lin et al.* [2014a], we plot  $Q_p$  perturbations versus  $V_p$  and  $V_p/V_s$  perturbations at the tomographic inversion nodes between 1 and 12 km depth where the diagonal elements of the resolution matrices of the  $Q_p$ ,  $V_p$  and  $V_p/V_s$  models are all greater than 0.1. The perturbations are calculated relative to the layer average values for all the three parameters. Figures 10a and 10b generally show scatter with no obvious correlations between  $Q_p$  and  $V_p$  or  $V_p/V_s$ , although low- $Q_p$  values show a slight dominance and a slight correlation with  $V_p/V_s$  ratios at 1 km depth.

We also plot  $Q_p$  perturbations versus  $V_p$  and  $V_p/V_s$  perturbations at earthquake hypocenters whose depths are  $\pm 1$  km across the tomographic inversion nodes (Figures 10c and 10d). Note that the perturbations are calculated relative to the layer-averaged values of the corresponding inversion nodes. Although the positive  $Q_p$  perturbations go up to 120%, low- $Q_p$  values take up 62% of all the events, indicating that seismicity has a preference for low  $Q_p$  values.

These plots show that in the active magmatic system of Kilauea, the 3-D  $Q_p$  structure is not correlated with the velocity model. We attribute this to the intrinsic effects (e.g., composition and density) on seismic velocities and strong dependence of attenuation on temperature, which is much more dominating in volcanoes.

### 6.6. Frequency Dependence and Scattering

In this study, we interpret our observed  $t^*$  variations purely in terms of a frequency-independent intrinsic  $Q_p$  model. However, previous studies have shown that  $Q$  can exhibit strong dependence on frequency between 1 and 10 Hz [e.g., *Adams and Abercrombie*, 1998; *Boatwright et al.*, 2002; *Erickson et al.*, 2004], although displaying no or weak frequency dependence above 10 Hz [e.g., *Adams and Abercrombie*,

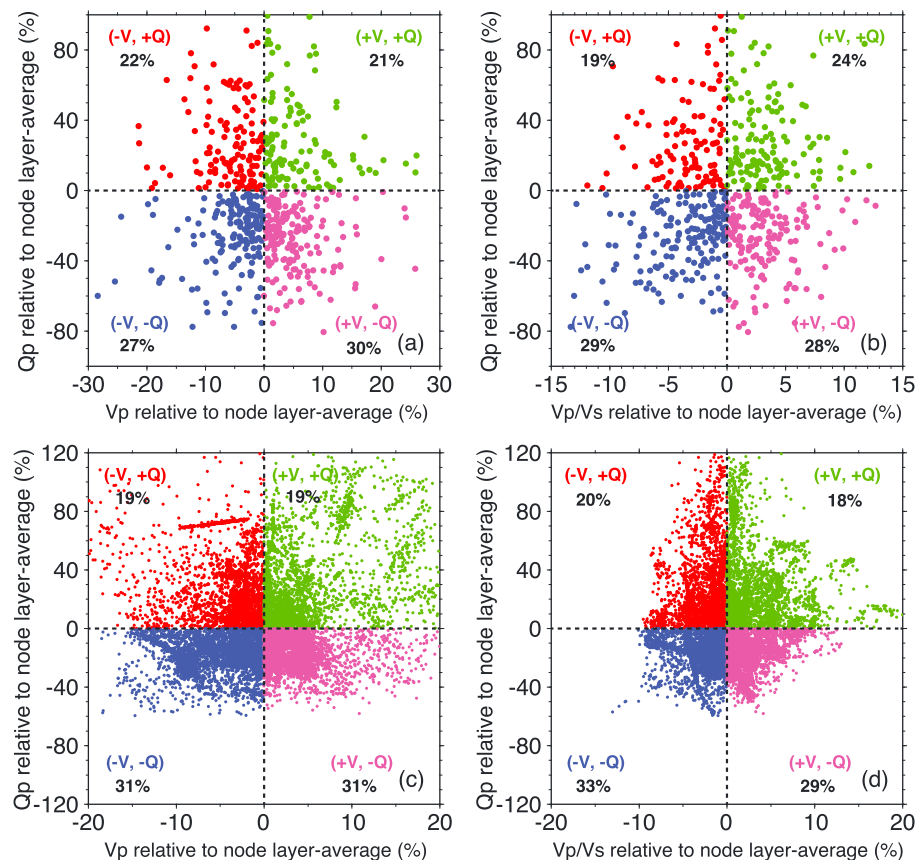


**Figure 10.** (a, b)  $Q_p$  perturbations versus  $V_p$  and  $V_p/V_s$  perturbations at the well-resolved inversion nodes. Perturbations are calculated relative to the layer average values for all the three parameters. (c, d)  $Q_p$  perturbations versus  $V_p$  and  $V_p/V_s$  perturbations at the well-resolved earthquake hypocenters whose depths are  $\pm 1$  km of the inversion layer depths. Perturbations are calculated relative to the layer average values of the corresponding grid nodes. Dots are colored by signs of the  $Q_p$  and velocity perturbations. Fractions show the percentage of grids in Figures 10a and 10b or events Figures 10c and 10d in each block.

1998; Prejean and Ellsworth, 2001]. In the frequency-dependent range, a power law relationship between attenuation and frequency is usually assumed by  $Q = Q_0 f^\eta$  [e.g., Anderson and Given, 1982; Toksoz et al., 1987], where  $f$  is the central frequency of the frequency dependence band and  $\eta$  is a constant between 0 (equivalent to frequency independence) and 1. Therefore, the  $Q_p$  model presented in this study should not be directly compared with frequency-dependent models. Note that in addition to intrinsic attenuation, scattering attenuation also contributes to our observed amplitude spectra decay. Frankel [1991] shows that in the frequency range of our study, the observed attenuation is caused about equally by scattering and intrinsic attenuation in three different tectonic areas. The proportion between these two may be different in our study area. Unfortunately, we do not have sufficient bandwidth to reliably distinguish these effects. Our model should be considered as a first-order measurement of the attenuation in Kilauea and can also be used as a starting point for future frequency-dependent attenuation studies.

## 7. Conclusions

In this paper, we present a newly developed frequency-independent 3-D  $Q_p$  model for Kilauea Volcano, Hawai'i, by inverting  $t^*$  values using the simul2000 tomographic algorithm. The low- $Q_p$  area and active seismicity throughout the entire depth range beneath the summit define the path of the magma ascent. We observe low- $Q_p$  values at shallow depths (above 4 km) in the rift zones, which may be mainly attributed to the shallow intrusions. Both the Southwest and East Rift Zones are dominated by very high  $Q_p$  values (up to 1000) at  $\sim 9$  km depth, which indicate cooled magma or highly competent material that controls the magma ascent and evolution in Kilauea Volcano. We do not observe obvious correlations between the 3-D  $Q_p$

values and the  $V_p$  or  $V_p/V_s$  models. Active seismicity seems to be correlated with low- $Q_p$  values. The availability of the 3-D  $Q_p$  model provides a complementary description of the volcanic feeding system to the existing velocity models.

#### Acknowledgments

We thank the HVO staff for maintaining the seismic data and Clifford H. Thurber for his simul2000 program. We are grateful to Matthew M. Haney and an anonymous reviewer for their constructive and detailed comments. Figures were made using the public domain GMT software [Wessel and Smith, 1991] and MATLAB. Funding for this research was provided by the National Science Foundation grant EAR-1246935.

#### References

- Adams, D. A., and R. E. Abercrombie (1998), Seismic attenuation above 10 Hz in Southern California from coda waves recorded in the Cajon Pass borehole, *J. Geophys. Res.*, *103*(B10), 24,257–24,270.
- Alexandrov, K. S., and T. V. Ryzhova (1961), Elastic properties of rock forming minerals: 1. Pyroxenes and amphiboles [Engl. Transl.], *Bull. Acad. Sci. USSR Geophys. Ser.*, *9*, 1165–1168.
- Amelung, F., S.-H. Yun, T. R. Walter, P. Segall, and S.-W. Kim (2007), Stress control of deep rift intrusion at Mauna Loa Volcano, Hawaii, *Science*, *316*(5827), 1026–1030, doi:10.1126/science.1140035.
- Anderson, D., and J. Given (1982), Absorption band Q model for the Earth, *J. Geophys. Res.*, *87*, 3893–3904.
- Anderson, J. G., and S. E. Hough (1984), A model for the shape of the Fourier amplitude spectrum of acceleration at high frequencies, *Bull. Seismol. Soc. Am.*, *74*(5), 1969–1993.
- Baker, S., and F. Amelung (2012), Top-down inflation and deflation at the summit of Kilauea Volcano, Hawaii observed with InSAR, *J. Geophys. Res.*, *117*, B12406, doi:10.1029/2011JB009123.
- Bennington, N., C. Thurber, and S. Roecker (2008), Three-dimensional seismic attenuation structure around the SAFOD site, Parkfield, California, *Bull. Seismol. Soc. Am.*, *98*(6), 2934–2947.
- Boatwright, J., G. L. Choy, and L. C. Seekins (2002), Regional estimates of radiated seismic energy, *Bull. Seismol. Soc. Am.*, *92*(4), 1241–1255.
- Brooks, B. A., J. Foster, D. Sandwell, C. J. Wolfe, P. Okubo, M. Poland, and D. Myer (2008), Magmatically triggered slow slip at Kilauea Volcano, Hawaii, *Science*, *321*(5893), 1177–1177, doi:10.1126/science.1159007.
- Brune, J. N. (1970), Tectonic stress and the spectra of seismic shear waves from earthquakes, *J. Geophys. Res.*, *75*(26), 4997–5009.
- Cayol, V., J. Dieterich, A. Okamura, and A. Miklius (2000), High magma storage rates before the 1983 eruption of Kilauea, Hawaii, *Science*, *288*(5475), 2343–2346.
- Christensen, N. I. (1996), Poisson's ratio and crustal seismology, *J. Geophys. Res.*, *101*(B2), 3139–3156.
- Christensen, N. I., and W. D. Mooney (1995), Seismic velocity structure and composition of the continental crust: A global view, *J. Geophys. Res.*, *100*(B7), 9761–9788.
- Clawson, S. R., R. B. Smith, and H. M. Benz (1989), P wave attenuation of the Yellowstone Caldera from three-dimensional inversion of spectral decay using explosion source seismic data, *J. Geophys. Res.*, *94*(B6), 7205–7222, doi:10.1029/JB094iB06p07205.
- Dawson, P. B., B. A. Chouet, P. G. Okubo, A. Villaseñor, and H. M. Benz (1999), Three-dimensional velocity structure of the Kilauea caldera, Hawaii, *Geophys. Res. Lett.*, *26*(18), 2805–2808.
- De Gori, P., C. Chiarabba, and D. Patanè (2005),  $Q_p$  structure of Mount Etna: Constraints for the physics of the plumbing system, *J. Geophys. Res.*, *110*, B05303, doi:10.1029/2003JB002875.
- De Siena, L., E. Del Pezzo, F. Bianco, and A. Tramelli (2009), Multiple resolution seismic attenuation imaging at Mt. Vesuvius, *Phys. Earth Planet. Inter.*, *173*, 17–32, doi:10.1016/j.pepi.2008.10.015.
- Del Pezzo, E., F. Bianco, L. De Siena, and A. Zollo (2006), Small scale shallow attenuation structure at Mt. Vesuvius, Italy, *Phys. Earth Planet. Inter.*, *157*, 257–268, doi:10.1016/j.pepi.2006.04.009.
- Eberhart-Phillips, D. (1986), Three-dimensional velocity structure in the northern California Coast Ranges from inversion of local earthquake arrival times, *Bull. Seismol. Soc. Am.*, *76*(4), 1025–1052.
- Eberhart-Phillips, D. (1993), Local earthquake tomography: Earthquake source regions, in *Seismic Tomography: Theory and Practice*, edited by H. M. Iyer and K. Hirahara, pp. 613–643, Chapman and Hall, London.
- Eberhart-Phillips, D., and M. Chadwick (2002), Three-dimensional attenuation model of the shallow Hikurangi subduction zone in the Raukumara Peninsula, New Zealand, *J. Geophys. Res.*, *107*(B2), 2033, doi:10.1029/2000JB000046.
- Eberhart-Phillips, D., and A. J. Michael (1993), Three-dimensional velocity structure, seismicity, and fault structure in the Parkfield region, central California, *J. Geophys. Res.*, *98*(B9), 15,737–15,758.
- Ellsworth, W., and R. Koyanagi (1977), Three-dimensional crust and mantle structure of Kilauea Volcano, Hawaii, *J. Geophys. Res.*, *82*(33), 5379–5394.
- Erickson, D., D. E. McNamara, and H. M. Benz (2004), Frequency-dependent  $Lg$  Q within the continental United States, *Bull. Seismol. Soc. Am.*, *94*(5), 1630–1643.
- Evans, J. R., and J. J. Zucca (1988), Active high-resolution seismic tomography of compressional wave velocity and attenuation structure at Medicine Lake Volcano, Northern California Cascade Range, *J. Geophys. Res.*, *93*(B12), 15,016–15,036.
- Frankel, A. (1991), Mechanisms of seismic attenuation in the crust: Scattering and anelasticity in New York state, South Africa, and Southern California, *J. Geophys. Res.*, *96*(B4), 6269–6289, doi:10.1029/91JB00192.
- Got, J.-L., V. Monteuil, J. Monteuil, R. Hassani, and P. Okubo (2008), Deformation and rupture of the oceanic crust may control growth of Hawaiian volcanoes, *Nature*, *451*(7177), 453–456, doi:10.1038/nature06481.
- Hansen, S., C. Thurber, M. Mandernach, F. Haslinger, and C. Doran (2004), Seismic velocity and attenuation structure of the East Rift Zone and south flank of Kilauea Volcano, Hawaii, *Bull. Seismol. Soc. Am.*, *94*(4), 1430–1440.
- Haslinger, F., C. Thurber, M. Mandernach, and P. Okubo (2001), Tomographic image of P-velocity structure beneath Kilauea's east rift zone and south flank: Seismic evidence for a deep magma body, *Geophys. Res. Lett.*, *28*(2), 375–378.
- Hauksson, E., and P. M. Shearer (2006), Attenuation models ( $Q_p$  and  $Q_s$ ) in three dimensions of the southern California crust: Inferred fluid saturation at seismogenic depth, *J. Geophys. Res.*, *111*, B05302, doi:10.1029/2005JB003947.
- Hill, D. P. (1969), Crustal structure of the Island of Hawaii from seismic-refraction measurements, *Bull. Seismol. Soc. Am.*, *59*(1), 101–130.
- Hill, D. P., and J. J. Zucca (1987), Geophysical constraints on the structure of Kilauea and Mauna Loa Volcanoes and some implications for seismomagmatic processes, *U.S. Geol. Surv. Prof. Pap.*, *1350*, 903–917.
- Hill, D. P., F. Pollitz, and C. Newhall (2002), Earthquake–Volcano interactions, *Phys. Today*, *55*(11), 41–47.
- Ho-Liu, P. H.-Y. (1988), Attenuation tomography. Modelling regional love waves: Imperial Valley to Pasadena, PhD dissertation, Calif. Inst. of Technol., Pasadena.
- Jackson, D. D., and D. L. Anderson (1970), Physical mechanisms of seismic-wave attenuation, *Rev. Geophys. Space Phys.*, *8*(1), 1–63.
- Kauahikaua, J., D. B. Jackson, and C. J. Zabolcki (1986), Resistivity structure to a depth of 5 km beneath Kilauea Volcano, Hawaii from large-loop-source electromagnetic measurements (0.04–8 Hz), *J. Geophys. Res.*, *91*(B8), 8267–8283, doi:10.1029/JB091iB08p08267.

- Kern, H. (1982), Elastic-wave velocity in crustal and mantle rocks at high pressure and temperature: The role of the high-low quartz transition and of dehydration reactions, *Phys. Earth Planet. Inter.*, *29*, 12–23.
- Lee, C.-T. A. (2003), Compositional variation of density and seismic velocities in natural peridotites at STP conditions: Implications for seismic imaging of compositional heterogeneities in the upper mantle, *J. Geophys. Res.*, *108*(B9), 2441, doi:10.1029/2003JB002413.
- Lees, J. M. (2007), Seismic tomography of magmatic systems, *J. Volcanol. Geotherm. Res.*, *167*, 37–56.
- Lin, G. (2013), Three-dimensional seismic velocity structure and precise earthquake relocations in the Salton Trough, southern California, *Bull. Seismol. Soc. Am.*, *103*(5), 2694–2708, doi:10.1785/0120120286.
- Lin, G. (2014a), Three-dimensional compressional wave attenuation tomography for the crust and uppermost mantle of northern and central California, *J. Geophys. Res.*, *119*, 3462–3477, doi:10.1002/2013JB010621.
- Lin, G. (2014b), Three-dimensional compressional attenuation model (Qp) for the Salton Trough, Southern California, *Bull. Seismol. Soc. Am.*, *104*(5), 2579–2586.
- Lin, G., and C. H. Thurber (2012), Seismic velocity variations along the rupture zone of the 1989 Loma Prieta earthquake, California, *J. Geophys. Res.*, *117*, B09301, doi:10.1029/2011JB009122.
- Lin, G., P. M. Shearer, E. Hauksson, and C. H. Thurber (2007), A three-dimensional crustal seismic velocity model for southern California from a composite event method, *J. Geophys. Res.*, *112*, B11306, doi:10.1029/2007JB004977.
- Lin, G., C. H. Thurber, H. Zhang, E. Hauksson, P. M. Shearer, F. Waldhauser, T. M. Brocher, and J. Hardebeck (2010), A California statewide three-dimensional seismic velocity model from both absolute and differential times, *Bull. Seismol. Soc. Am.*, *100*(1), 225–240, doi:10.1785/0120090028.
- Lin, G., P. M. Shearer, R. S. Matoza, P. G. Okubo, and F. Amelung (2014a), Three-dimensional seismic velocity structure of Mauna Loa and Kilauea Volcanoes in Hawaii from local seismic tomography, *J. Geophys. Res. Solid Earth*, *119*, 4377–4392, doi:10.1002/2013JB010820.
- Lin, G., F. Amelung, Y. Lavallee, and P. G. Okubo (2014b), Seismic evidence for a crustal magma reservoir beneath the Upper East Rift Zone of Kilauea Volcano, Hawaii, *Geology*, *42*, 187–190, doi:10.1130/G35001.1.
- Lipman, P., J. Lockwood, R. Okamura, D. Swanson, and K. Yamashita (1985), Ground deformation associated with the 1975 magnitude-7.2 earthquake and resulting changes in activity of Kilauea Volcano, Hawaii, *U.S. Geol. Surv. Prof. Pap.*, *1276*, 1–45.
- Martinez-Arevalo, C., D. Patane, A. Rietbrock, and J. Ibanez (2005), The intrusive process leading to the Mt. Etna 2001 flank eruption: Constraints from 3-D attenuation tomography, *Geophys. Res. Lett.*, *32*, L21309, doi:10.1029/2005GL023736.
- Monteiller, V., J. Got, J. Virieux, and P. Okubo (2005), An efficient algorithm for double-difference tomography and location in heterogeneous media, with an application to the Kilauea Volcano, *J. Geophys. Res.*, *110*, B12306, doi:10.1029/2004JB003466.
- Nakajima, J., S. Hada, E. Hayami, N. Uchida, A. Hasegawa, S. Yoshioka, T. Matsuzawa, and N. Umino (2013), Seismic attenuation beneath northeastern Japan: Constraints on mantle dynamics and arc magmatism, *J. Geophys. Res. Solid Earth*, *118*, 5838–5855, doi:10.1002/2013JB010388.
- Ohlendorf, S. J., C. H. Thurber, J. D. Pesicek, and S. G. Prejean (2014), Seismicity and seismic structure at Okmok Volcano, Alaska, *J. Volcanol. Geotherm. Res.*, *278–279*, 103–119, doi:10.1016/j.jvolgeores.2014.04.002.
- Okubo, P. G., H. M. Benz, and B. A. Chouet (1997), Imaging the crustal magma sources beneath Mauna Loa and Kilauea Volcanoes, Hawaii, *Geology*, *25*(10), 867–870.
- Park, J., J. K. Morgan, C. A. Zelt, P. G. Okubo, L. Peters, and N. Benesh (2007), Comparative velocity structure of active Hawaiian volcanoes from 3-D onshore-offshore seismic tomography, *Earth Planet. Sci. Lett.*, *259*(3–4), 500–516, doi:10.1016/j.epsl.2007.05.008.
- Park, J., J. K. Morgan, C. A. Zelt, and P. G. Okubo (2009), Volcano-tectonic implications of 3-D velocity structures derived from joint active and passive source tomography of the island of Hawaii, *J. Geophys. Res.*, *114*, B09301, doi:10.1029/2008JB005929.
- Pavlis, G. L., and J. R. Booker (1980), The mixed discrete-continuous inverse problem: Application to the simultaneous determination of earthquake hypocenters and velocity structure, *J. Geophys. Res.*, *85*(B9), 4801–4810.
- Pietruszka, A., and M. Garcia (1999), The size and shape of Kilauea Volcano's summit magma storage reservoir: A geochemical probe, *Earth Planet. Sci. Lett.*, *167*(3–4), 311–320.
- Poland, M. P., A. Miklius, and E. K. Montgomery-Brown (2014), Magma supply, storage, and transport at shield-stage Hawaiian volcanoes, in *Characteristics of Hawaiian Volcanoes*, edited by M. P. Poland, T. J. Takahashi, and C. M. Landowski, *U.S. Geol. Surv. Prof. Pap.* *1801*, 179–234.
- Ponko, S. C., and C. O. Sanders (1994), Inversion for P and S wave attenuation structure, Long Valley caldera, California, *J. Geophys. Res.*, *99*(B2), 2619–2635, doi:10.1029/93JB03405.
- Prejean, S. G., and W. L. Ellsworth (2001), Observations of earthquake source parameters at 2 km depth in the Long Valley Caldera, Eastern California, *Bull. Seismol. Soc. Am.*, *91*(2), 165–177.
- Prieto, G. A., R. L. Parker, and F. L. Vernon (2009), A Fortran 90 library for multitaper spectrum analysis, *Comput. Geosci.*, *35*(8), 1701–1710, doi:10.1016/j.cageo.2008.06.007.
- Rietbrock, A. (2001), P wave attenuation structure in the fault area of the 1995 Kobe earthquake, *J. Geophys. Res.*, *106*(B3), 4141–4154.
- Rowan, L., and R. W. Clayton (1993), The three-dimensional structure of Kilauea Volcano, Hawaii, from travel time tomography, *J. Geophys. Res.*, *98*(B3), 4355–4375.
- Rubin, A., D. Gillard, and J. Got (1998), A reinterpretation of seismicity associated with the January 1983 dike intrusion at Kilauea Volcano, Hawaii, *J. Geophys. Res.*, *103*(B5), 10,003–10,015.
- Ryall, A., and D. L. Bennett (1968), Crustal structure of Southern Hawaii related to volcanic processes in the upper mantle, *J. Geophys. Res.*, *73*(14), 4561–4582.
- Sanders, C., S. Ponko, L. Nixon, and E. Schwartz (1994), Local earthquake attenuation and velocity tomography for magmatic and hydrothermal structure in Long Valley Caldera, Calif., *Seismol. Res. Lett.*, *65*(1), 56.
- Sanders, C. O. (1993), Reanalysis of S-to-P amplitude ratios for gross attenuation structure, Long Valley Caldera, Calif., *J. Geophys. Res.*, *98*(B12), 22,069–22,079.
- Sanders, C. O., and L. D. Nixon (1995), S wave attenuation structure in Long Valley caldera, California, from three-component S-to-P amplitude ratio data, *J. Geophys. Res.*, *100*(B7), 12,395–12,404.
- Sanders, C. O., S. C. Ponko, L. D. Nixon, and E. A. Schwartz (1995), Seismological evidence for magmatic and hydrothermal structure in Long Valley caldera from local earthquake attenuation and velocity tomography, *J. Geophys. Res.*, *100*(B5), 8311–8326.
- Scherbaum, F., and M. Wyss (1990), Distribution of attenuation in the Koaiki, Hawaii, source volume estimated by inversion of wave spectra, *J. Geophys. Res.*, *95*(B8), 12,439–12,448.
- Spencer, C., and D. Gubbins (1980), Travel-time inversion for simultaneous earthquake location and velocity structure determination in laterally varying media, *Geophys. J. R. Astron. Soc.*, *63*(1), 95–116.
- Swanson, D., W. Duffield, and R. Fiske (1976a), Displacement of the south flank of Kilauea Volcano; The result of forceful intrusion of magma into the rift zones, *U.S. Geol. Surv. Prof. Pap.*, *963*, 1–30.

- Swanson, D., D. Jackson, R. Koyanagi, and T. Wright (1976b), The February 1969 east rift eruption of Kilauea Volcano, Hawaii, *U.S. Geol. Surv. Prof. Pap.*, 891, 30.
- Syracuse, E. M., C. H. Thurber, C. J. Wolfe, P. G. Okubo, J. H. Foster, and B. A. Brooks (2010), High-resolution locations of triggered earthquakes and tomographic imaging of Kilauea Volcano's south flank, *J. Geophys. Res.*, 115, B10310, doi:10.1029/2010JB007554.
- Thurber, C. (1984), Seismic detection of the summit magma complex of Kilauea Volcano, Hawaii, *Science*, 223(4632), 165–167.
- Thurber, C., and D. Eberhart-Phillips (1999), Local earthquake tomography with flexible gridding, *Comput. Geosci.*, 25, 809–818.
- Thurber, C., H. Zhang, T. Brocher, and V. E. Langenheim (2009), Regional three-dimensional seismic velocity model of the crust and uppermost mantle of Northern California, *J. Geophys. Res.*, 114, B01304, doi:10.1029/2008JB005766.
- Thurber, C. H. (1987), Seismic structure and tectonics of Kilauea Volcano, *U.S. Geol. Surv. Prof. Pap.*, 1350, 919–934.
- Thurber, C. H. (1993), Local earthquake tomography: Velocities and  $V_p/V_s$ -theory, in *Seismic Tomography: Theory and Practice*, edited by H. M. Iyer and K. Hirahara, pp. 563–583, Chapman and Hall, London.
- Toksoz, M., R. S. Wu, and D. P. Schmitt (1987), Physical mechanisms contributing to seismic attenuation in the crust, in *Proc. NATO ASI "Strong Ground Motion Seisraology," Ankara, Turkey*, edited by M. Erdik, and M. N. Toksöz, pp. 225–247, D. Reidel, Dordrecht, Netherlands.
- Trampert, J., P. Vacher, and N. Vlaar (2001), Sensitivities of seismic velocities to temperature, pressure and composition in the lower mantle, *Phys. Earth Planet. Inter.*, 124(3–4), 255–267.
- Wessel, P., and W. H. F. Smith (1991), Free software helps map and display data, *Eos Trans. AGU*, 72, 441–446.
- Winkler, K., and A. Nur (1979), Pore fluids and seismic attenuation in rocks, *Geophys. Res. Lett.*, 6, 1–4.
- Zucca, J., and J. Evans (1992), Active high-resolution compressional wave attenuation tomography at Newberry Volcano, central Cascade Range, *J. Geophys. Res.*, 97, 11,047–11,055.